Contents lists available at ScienceDirect

Journal of Rock Mechanics and Geotechnical Engineering

Full Length Article

Influence of heterogeneity on rock strength and stiffness using discrete element method and parallel bond model

Spyridon Liakas [a], Catherine O'Sullivan [b], Charalampos Saroglou [c],*

[a] *Arup Geotechnics, Solihull, UK*
[b] *Department of Civil & Environmental Engineering, Imperial College London, London, UK*
[c] *Department of Geotechnical Engineering, School of Civil Engineering, National Technical University Athens, Athens, Greece*

ABSTRACT

The particulate discrete element method (DEM) can be employed to capture the response of rock, provided that appropriate bonding models are used to cement the particles to each other. Simulations of laboratory tests are important to establish the extent to which those models can capture realistic rock behaviors. Hitherto the focus in such comparison studies has either been on homogeneous specimens or use of two-dimensional (2D) models. In situ rock formations are often heterogeneous, thus exploring the ability of this type of models to capture heterogeneous material behavior is important to facilitate their use in design analysis. In situ stress states are basically three-dimensional (3D), and therefore it is important to develop 3D models for this purpose. This paper revisits an earlier experimental study on heterogeneous specimens, of which the relative proportions of weaker material (siltstone) and stronger, harder material (sandstone) were varied in a controlled manner. Using a 3D DEM model with the parallel bond model, virtual heterogeneous specimens were created. The overall responses in terms of variations in strength and stiffness with different percentages of weaker material (siltstone) were shown to agree with the experimental observations. There was also a good qualitative agreement in the failure patterns observed in the experiments and the simulations, suggesting that the DEM data enabled analysis of the initiation of localizations and micro fractures in the specimens.
© 2017 Institute of Rock and Soil Mechanics, Chinese Academy of Sciences. Production and hosting by Elsevier B.V. This is an open access article under the CC BY-NC-ND license (http://creativecommons.org/licenses/by-nc-nd/4.0/).

1. Introduction

This study explores the use of discrete element method (DEM) to capture the influence of weak interlayers on the overall response of heterogeneous rock specimens. The bonded particle model (BPM) proposed by Potyondy and Cundall (2004) was used to simulate the heterogeneous rocks made up of layers of two different lithological units with significant differences in strength and stiffness. A comparison of the DEM simulation data with the results from a prior experimental study (Tziallas et al., 2013) shows that the model can capture reasonably the variation of strength with increasing proportion of the weaker materials. The influence of relative strengths of lithological units of the heterogeneous rocks on the overall strengths and stiffnesses

of the composite heterogeneous rock specimens was also investigated.

This paper first gives an overview of the mechanical responses of composite rocks, and then the simulation approach is presented. The analysis of the results also considers the overall material response prior to discussing the particle-scale mechanics.

2. Background

2.1. Mechanical behaviors of composite rocks

The composition and structure of rocks are altered by natural geological processes leading to the formation of heterogeneous rock masses with complex engineering behaviors. Heterogeneous rocks are usually of sedimentary origin and consist of relatively stronger and weaker rock alternately with varying thickness. Complex geological formations such as turbidites, flysch and molasses are typical examples of such rocks.

Researchers including Hoek (1968), Hawkes and Mellor (1970), Paterson and Wong (2005) and Kwaśniewski et al. (2012)

---

* Corresponding author.
E-mail address: saroglou@central.ntua.gr (C. Saroglou).
Peer review under responsibility of Institute of Rock and Soil Mechanics, Chinese Academy of Sciences.

amongst others have experimentally studied the failure modes of rocks. Tang and Hudson (2010) stated that the failure of brittle rocks under uniaxial compression was due to the expansion of the initial micro cracks to a major shear band, whereas in confined tests the failure can be attributed to the coalescence of the micro fractures into a critical shear failure zone. At higher confining pressure, the Young's modulus and the peak strength values of rocks are higher and a transition from brittle to ductile deformation occurs.

The effect of heterogeneity on the failure mode was studied by Liang et al. (2007) and Tziallas et al. (2013) through conducting uniaxial compression tests on the composite specimens with varying siltstone-sandstone ratios as illustrated in Fig. 1. They observed that the failure mode was affected by the proportion of the weaker materials (siltstone). For specimens with lower values of siltstone percentage, extensional fractures were formed throughout the specimens, whereas for specimens with higher values, the fractures were merely restricted to the weaker materials. Liang et al. (2007) conducted triaxial tests on composite specimens of anhydrite (stronger, harder component) and halite (weaker component) and they observed that there was a strain incompatibility along the interface leading to tensile or shear cracking in the harder component and more ductile deformation in the weaker component. Greco et al. (1991) also investigated the strength and failure mechanism of composite rock specimens subjected to uniaxial compression. According to their investigation, tests on specimens composed of discs of the same material resulted in lower uniaxial compressive strength (10% reduction) compared to continuous specimens. In their laboratory tests on composite specimens of shale and sandstone, Mohamed et al. (2007) studied the effect of the thickness of shale on the overall strength. They concluded that for specimens with shale percentage greater than 10%, the strength of the composite specimen was equal to the strength of the weaker material. Vergara et al. (2015) performed large-scale triaxial test on bedded sandstone–claystone specimens, and concluded that the failure of the bedded specimens occurred by a combined failure of both materials in a ductile manner. They also conducted a numerical analysis using a two-dimensional (2D) universal distinct element code (UDEC) to simulate the specimens composed of alternating layers of both materials with equal thickness. It was shown that when confining pressure was less than 15 MPa, the strength of the specimen was controlled by tensile failure of the harder rock, while under larger confining pressure,

the strength was controlled by shear failure of the weaker rock. Lin et al. (2013) studied the anisotropic behavior of a layered rock mass under triaxial compression using a three-dimensional finite element method (3D FEM) for numerical analysis. Anisotropy due to the presence of bedding planes affects the failure pattern of transversely isotropic, heterogeneous rocks. The varying inclination of the bedding planes relative to the major loading axis affects both their strength and failure mode (Tien et al., 2006).

2.2. Use of bonded particle model to simulate the behavior of rock mass

The particulate DEM was originally proposed for fundamental simulations of unbonded granular materials by Cundall and Strack (1979). This algorithm can be applied to analyzing the behavior of rock mass using contact models that can transmit tensile forces. The parallel bond model (PBM), documented by Potyondy and Cundall (2004), is a relatively sophisticated bonding model that enables specification of tensile and shear strengths. The bonds are of finite size and thus there is moment transfer/resistance due to the normal and tangential components of the contact force. A number of studies have reported the use of this model to simulate rock mass behavior. Studies using 2D model such as Cho et al. (2007) provide useful qualitative insight into the model's behavior; however, effective models should reflect the 3D nature of the physical material. Potyondy and Cundall (2004) reported only limited success in simulating the behavior of Lac du Bonnet granite. However, Potyondy (2007) found that a modified PBM, the parallel-bonded stress corrosion (PSC) model, could successfully reproduce experimental data from static fatigue tests. Zhang et al. (2011) calibrated DEM specimens using the PBM along with a fracture model to capture the response of Yamaguchi marble and they succeeded in capturing the size dependency of the uniaxial compressive strength observed in laboratory tests. Cheung et al. (2013) performed a parametric study to illustrate how the PBM parameters influence the overall behavior, prior to describing a relatively successful calibration of the PBM to simulate the response of Castlegate and Saltwash sandstones; the load–deformation response of the model agreed with experimental data until the peak stress was mobilized. Nevertheless for the post-peak regime, the model was less successful.

There have been some 2D DEM simulations that have explored the issues of layering and inhomogeneity. Park and Min (2015) used a 2D DEM modeling approach that included embedded smooth joints to simulate the mechanical behavior of a transversely isotropic rock using the PBM. They compared the laboratory observations of model behaviors of three rock types (gneiss, shale and schist) and concluded that this modeling approach can successfully capture the failure patterns observed in anisotropic rock in which weak planes play a significant role. Hsieh et al. (2008) conducted 2D DEM simulations using the BPM to study the relationship between the macroscopic properties of sandstones and their petrographic or microscopic properties. Jeng et al. (2008) also used 2D DEM to create a model of layered rock. In their work, they captured experimental observations of the influence of the layer inclination on strength and stiffness. They also explored the influence of the relative strengths and stiffnesses of the two materials on the overall behavior. However, these results were not linked to experimental data. In addition, Abe and Urai (2012) studied a layered rock material using 2D DEM simulations. These earlier studies have demonstrated the potential of the model and the current contribution aims to further develop confidence in the PBM by demonstrating its ability to capture known response features of heterogeneous rock specimens. In particular, an in situ 3D material subjected to a 3D stress state is of interest, and therefore the earlier
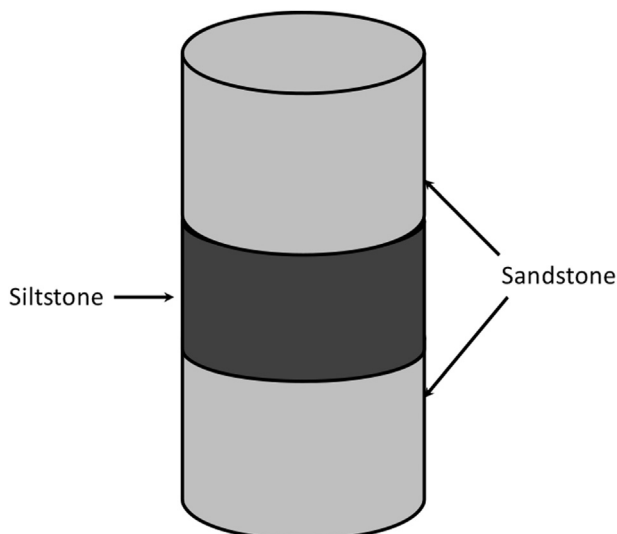

Fig. 1. Schematic of composite specimen configuration.

2D studies (Hsieh et al., 2008; Jeng et al., 2008; Abe and Urai, 2012) are extended here to represent rock heterogeneity in three dimensions.

3. Simulation approach

The DEM software PFC3D (Cheung et al., 2013) was used in the current study. The BPM of the rock mass was created using the PBM (Potyondy and Cundall, 2004) which was implemented in this software to bond or cement particles together. The DEM simulations of triaxial tests presented here are a direct extension of the earlier contributions by Cheung et al. (2013). In all cases, the specimens (40 mm in diameter, 80 mm in height) consisted of 12,622 spheres, with particle radii uniformly distributed between 0.88 mm and 1.32 mm, and a radius expansion technique was used to create the initial specimens. Similar to Cheung et al. (2013), the material density was increased to 26.5×10^3 kg/m^3 in order to increase the stable time increment and reduce the computational cost. Density scaling increases the time step and therefore reduces the simulation cost as the stable time step is proportional to $\sqrt{m/K}$, where m is the particle mass and K is the contact stiffness. Increasing the density in this manner will not affect the results, provided that the simulations are quasi-static, i.e. inertia effects are minimized and particle acceleration remains very small. The quasi-static nature of the simulations was verified by checking the overall equilibrium of forces in the system, i.e. it was confirmed that the reaction force generated on the bottom boundary was approximately equal to the force applied via the top boundary. To ensure reasonable model parameters and avoid the computationally expensive stage of model calibration against physical tests, the parameters used by Cheung et al. (2013) which had been calibrated against Castlegate sandstone were adopted. Cheung et al. (2013) calibrated the model parameters used in the simulations in terms of high pressure triaxial test data. To maintain the link to physical test specimens, the analyses carried out herein therefore also used a high confining pressure. The specimens were initially prepared using homogeneous material within a box of 0.1 m × 0.1 m × 0.2 m having rigid frictionless walls. The cylindrical specimens were then cut from this box to minimize the boundary effects and achieve more homogeneous specimens. The material properties for each layer were assigned after this process was completed. In this regard, the difference in contact parameters would not have a measurable effect on the contact force network. Furthermore, as the layers are orthogonal to the major principal stress and cover the entire specimen cross-section, no subsequent force chain redistribution would be expected. The specimens were compressed to an isotropic stress of 10 MPa and a confining pressure of 10 MPa was maintained in the strain-controlled triaxial shearing tests. Two rock types were considered to create the composite/heterogeneous specimens. Initially, a homogenous sandstone specimen with material properties identical to those used by Cheung et al. (2013) was considered, with the properties listed in Table 1. The normal and shear spring stiffnesses are given by K_n and K_s, respectively. The superscript 'C' denotes ball properties and the superscript 'PB' denotes parallel bond. The parallel bond strengths in the normal and shear directions are denoted by S_n^{PB} and S_s^{PB}, respectively. Then, following the experimental approach of Mohamed et al. (2007) and Tziallas et al. (2013), as illustrated in Fig. 1, the composite/heterogeneous specimens were created by inserting a siltstone disk in the center of the specimen and increasing this disk systematically so that the volume percentage of siltstone in the model rocks varied from 0% to 100% (10% increment in each step). In the DEM model, the siltstone was simulated by controlling the relative values of the parameters used to model the two rock types. For the DEM model, the contact model parameters for each existing contact were specified based on

Table 1
Simulation parameters used to vary model rock properties.

Rock	$q_{strong}^{max}/q_{weak}^{max}$	Ball properties	Parallel bond properties	
		K_n^C, K_s^C (kN/m)	K_n^{PB}, K_s^{PB} (kPa/m)	S_n^{PB}, S_s^{PB} (kPa)
Sandstone	1.75	6.286×10^3	8.27×10^8	5.2×10^4
	3.47	6.286×10^3	8.27×10^8	5.2×10^4
	5	1.572×10^4	2.086×10^9	1.3×10^5
Siltstone	1.75	2.389×10^3	3.143×10^8	2.363×10^4
	3.47	8.172×10^2	1.075×10^8	7.878×10^3
	5	1.886×10^3	2.481×10^8	1.576×10^4

Note: K_n^C, K_s^C = normal and shear contact stiffnesses, respectively; K_n^{PB}, K_s^{PB} = normal and shear parallel bond stiffnesses, respectively.

the contact elevation. As listed in Table 1, three cases were considered:

$$q_{strong}^{max}/q_{weak}^{max} = \begin{cases} 1.75 \\ 3.47 \\ 5 \end{cases} \quad (1)$$

where q_{strong}^{max} and q_{weak}^{max} are the maximum deviatoric stresses (i.e. the deviatoric stresses at peak) in homogeneous specimens of the harder, stronger sandstone material and the weaker siltstone material, respectively. The deviatoric stress is calculated as

$$q = \sigma_1 - \sigma_3 \quad (2)$$

where σ_1 is the major principal stress and σ_3 is the minor principal stress, which are obtained considering the boundary stresses.

The maximum deviatoric stress, q^{max}, is the maximum value of q obtained by considering the entire stress-history for each test. The values of q_{strong}^{max} and q_{weak}^{max} were obtained by considering the triaxial test simulation data for specimens composed entirely of the stronger or weaker material, respectively. As is clear from Table 1, the sandstone properties were the same for the simulations with $q_{strong}^{max}/q_{weak}^{max} = 1.75$ and 3.47. To ensure that similar trends would be observed with different model sandstones, the contact stress and stiffness parameters were increased in the sandstone for the simulation with $q_{strong}^{max}/q_{weak}^{max} = 5$. In all cases for sandstone and siltstone, a parallel bond radius of 1 times the smaller sphere diameter was used and the inter particle coefficient of friction was 0.25. A local damping coefficient of 0.7 was adopted and the critical time increment calculated by PFC3D was multiplied by 0.4 to increase the accuracy and reduce the risk of numerical instability.

4. Mechanical responses

Fig. 2 illustrates the variation in observed load−deformation response with the volume percentage of siltstone in the specimen (sl) for specimens with $q_{strong}^{max}/q_{weak}^{max}$ values of 1.75 and 5. Three regions of specimen's responses to stress change have been identified for the heterogeneous specimens. The characteristic stress−strain curve is linear up to a deviatoric stress very close to the peak strength of the weaker component. Beyond this point up to the peak stress, the curve deviates from linearity, indicating excessive shearing and bond failures in the middle weaker zone of the heterogeneous specimen. From the peak stress onwards, a rapid drop of the strength towards the strength of the weaker material is observed (with large strain). Referring to Fig. 2a, when $q_{strong}^{max}/q_{weak}^{max} = 1.75$, it is clear that the peak strength and the pre-peak specimen stiffness decrease with increasing sl while the differences in the stress−strain curve are smaller at large strain values ($\varepsilon_a > 8.5\%$). The axial strain (ε_a) at which the peak deviatoric stress is mobilized (axial strains at failure) increases from 3.3% ($sl = 0\%$) to 5.15% ($sl = 60\%$). However, when sl exceeds 60%, the subsequent
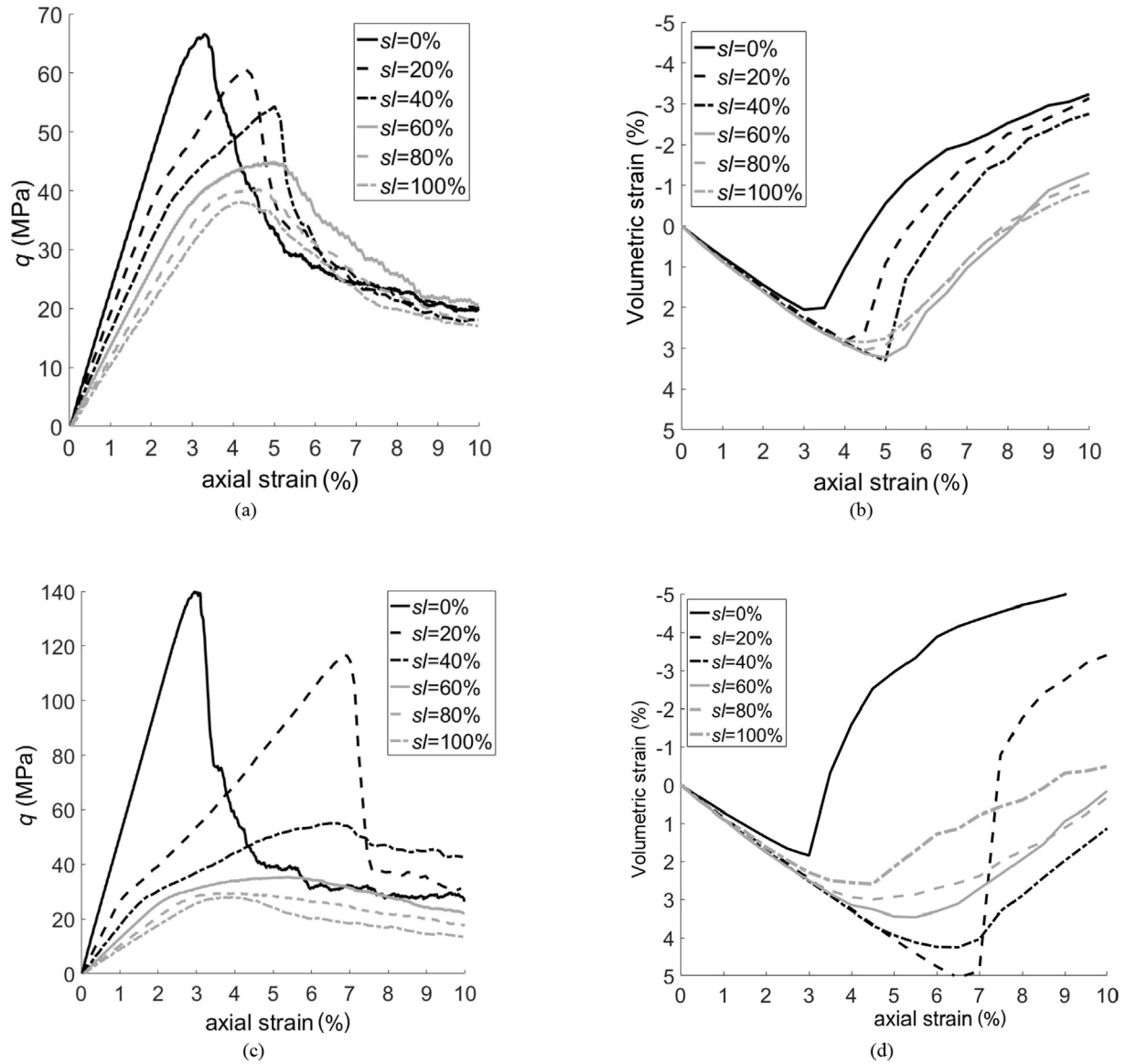
Fig. 2. Load-deformation response of composite specimens: (a) Deviatoric stress versus axial strain for $q_{strong}^{max}/q_{weak}^{max} = 1.75$, (b) Volumetric strain versus axial strain for $q_{strong}^{max}/q_{weak}^{max} = 1.75$, (c) Deviatoric stress versus axial strain for $q_{strong}^{max}/q_{weak}^{max} = 5$, and (d) Volumetric strain versus axial strain for $q_{strong}^{max}/q_{weak}^{max} = 5$ (*sl* is the percentage of siltstone in specimen).
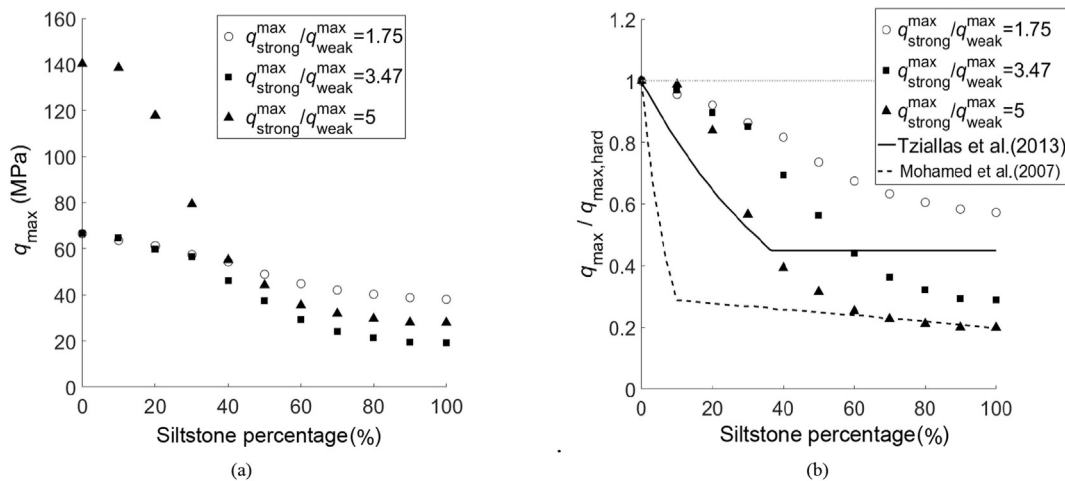
Fig. 3. (a) Variation in peak deviatoric stress with siltstone content for DEM data, and (b) Variation in normalized peak deviatoric stress with siltstone content and comparison of DEM results and experimental data.

increase in sl gives a reduction in the axial strain at failure. For specimens with $q_{strong}^{max}/q_{weak}^{max} = 5$ (see Fig. 2c) at low sl values (0% and 20%), the peak stress is significantly higher and the post-peak softening is more significant. However, for sl values of 40% and above, the strengths are similar to the case where $q_{strong}^{max}/q_{weak}^{max} = 1.75$, and the response of rock is no longer very brittle. Similarly, a significant reduction in the axial strains at failure occurs when sl exceeds 40%. The decrease of the brittleness as sl increases is also presented in Fig. 2b and d. The specimen contracts up to the axial strain at which the peak deviatoric stress is mobilized before the start of dilation.

Fig. 3a illustrates the peak deviatoric stress q_{max} against the percentage of siltstone (sl) for specimens with $q_{strong}^{max}/q_{weak}^{max}$ of 1.75, 3.47 and 5. As the simulations with $q_{strong}^{max}/q_{weak}^{max}$ of 1.75 and 3.47 have the same sandstone properties, the peak deviatoric stresses at a siltstone content of 0% are the same. The parallel bond and contact bond stiffnesses and the parallel bond strengths for the sandstone material are higher for the simulation with $q_{strong}^{max}/q_{weak}^{max} = 5$, suggesting higher deviatoric stress at lower siltstone content. For specimens with high siltstone content, the maximum deviatoric stresses are related to the strengths specified in the parallel bond

model. Referring to Table 1, the simulation with $q_{strong}^{max}/q_{weak}^{max}$ of 1.75 has the highest parallel bond strength, while the simulation with $q_{strong}^{max}/q_{weak}^{max}$ of 3.47 has the lowest. In Fig. 3b, the data are replotted with the maximum deviatoric stress values being normalized by the deviatoric stress at $sl = 0\%$ ($q_{max,\ hard}$). It is clear that the value of $q_{strong}^{max}/q_{weak}^{max}$ determines the sensitivity of the peak deviatoric stress to the siltstone content.

A more significant drop in deviatoric stress is observed when the ratio of sl is higher. When the siltstone content exceeds 40%, the deviatoric stress decreases dramatically due to a decrease in brittleness, and the behavior of the composite specimen becomes more ductile as the behavior of the siltstone dominates the composite response. Fig. 3b also includes laboratory data from Tziallas et al. (2013) and Mohamed et al. (2007). The experiments carried out by Mohamed et al. (2007) had a ratio of $q_{strong}^{max}/q_{weak}^{max} = 4.4$, while those performed by Tziallas et al. (2013) had a ratio of $q_{strong}^{max}/q_{weak}^{max} = 2.2$. In comparison with the physical tests, the DEM simulations give a more gradual decrease in the normalized maximum deviatoric stress with increasing percentage of weak material. However, it is interesting to note that at a qualitative level, the trends are very similar. Most notably for a given $q_{strong}^{max}/q_{weak}^{max}$ ratio, there is a point after which further increases in the percentage of weaker material do not cause an associated decrease in the maximum deviatoric stress. Additionally, this point occurs at gradually lower percentage of weaker material as the value $q_{strong}^{max}/q_{weak}^{max}$ increases, which was in agreement with the laboratory data. Referring to the experimental data, it is clear that the quantitative relation between the rock peak stress and the percentage of weaker material depends on the specific rock types considered, but the trends are similar for the two available experimental datasets. As the DEM model was not calibrated by any sets of experimental data, we would not expect the model to give an exact match to either of the two datasets. Thanks to this, these data supplement the earlier observation of Jeng et al. (2008) who suggested that 2D DEM can capture the influence of layer inclination as the DEM can capture the influence of the relative proportion of the weaker and stronger layers on the composite strength.

Fig. 4 illustrates the variation in normalized Young's modulus $E_a/E_{a,hard}$ (E_a is the Young's modulus of the composite specimens, and $E_{a,hard}$ is the Young's modulus of the harder, stronger material) versus the siltstone percentage for the three DEM simulation series considered. These data are compared with experimental results from Tziallas et al. (2013). In all cases, the E_a values of the composite specimen are normalized by the $E_{a,hard}$ value. There is a systematic reduction in the Young's modulus with increasing siltstone content,
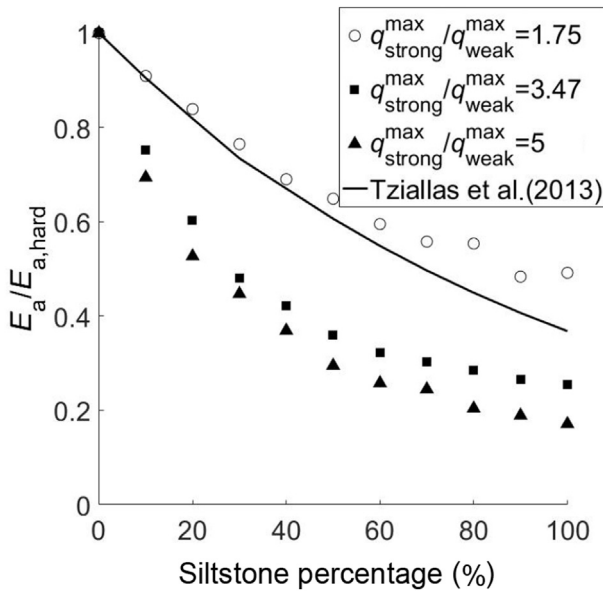

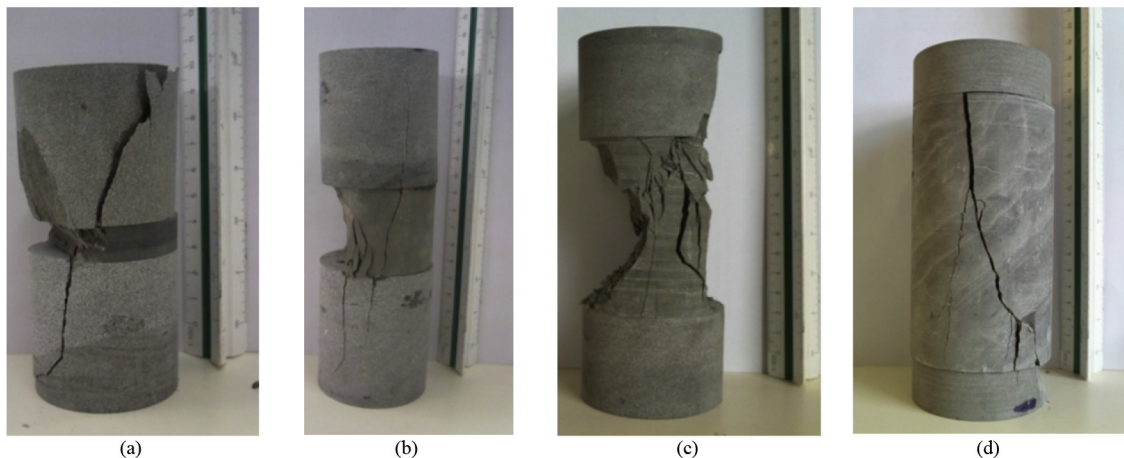Fig. 4. Variation in Young's modulus with siltstone percentage.

Fig. 5. Images of specimens after compression tests in Tziallas et al. (2013): (a) 10% siltstone, (b) 25% siltstone, (c) 47% siltstone, and (d) 75% siltstone.

and no apparent plateau is observed. The slope of the reduction is nonlinear in all cases, and the slope magnitude increases as $q_{\text{strong}}^{\max}/q_{\text{weak}}^{\max}$ value increases. Referring to Table 1, as $q_{\text{strong}}^{\max}/q_{\text{weak}}^{\max}$ value increases, the ratio of the contact stiffness and the parallel bond stiffness increases. In this case, there is a better agreement between the experimental and numerical data.

5. Failure patterns

The overall mechanical response is related to the development of damage in the rock. Images of representative laboratory specimens at the end of the tests in Tziallas et al. (2013) are provided in Fig. 5. As noted by Tziallas et al. (2013), at lower siltstone contents, there are clear brittle fractures and the fracture surfaces propagate through the entire specimen (Fig. 5a). As the siltstone content increases, the fracture pattern becomes more ductile and the cracks

form in the sandstone disks indicate propagation of the failure (Fig. 5b). With further increases in siltstone content as the composite strength approaches the strength of the siltstone material, the fracture concentrates in the siltstone, only propagating into the sandstone as faint cracks or (superficial) spalling (Fig. 5c and d).

Fig. 6 presents snapshots of the DEM specimens at the end of the simulations at siltstone contents similar to those considered in Fig. 5. In each case, a slice through the center of the specimen is considered and the particles are plotted as disks with the disk color indicating the amount of rotation (darker color corresponding to larger rotation). Particle rotations are often used in DEM simulations to identify localizations (e.g. O'Sullivan et al., 2003). The presence of the parallel bonds applies rotational restrictions to the bonded contacts and therefore, the particle rotations are concentrated in the areas where significant bond breakages take place. The local volumetric strain values at the same locations are considered
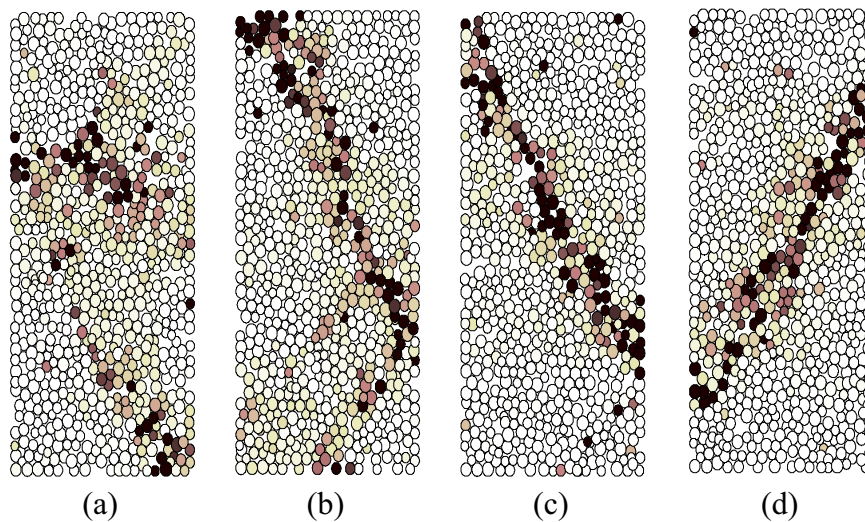

Fig. 6. Images of particle rotations at the end of tests with $q_{\text{strong}}^{\max}/q_{\text{weak}}^{\max} = 1.75$, where the darkest color gives the greatest rotation and color scaling is normalized for each plot: (a) 10% siltstone ($\varepsilon_a = 4\%$, $\varepsilon_a^{\text{peak}} = 3.8\%$), (b) 20% siltstone ($\varepsilon_a = 4.5\%$, $\varepsilon_a^{\text{peak}} = 4.3\%$), (c) 50% siltstone ($\varepsilon_a = 5.5\%$, $\varepsilon_a^{\text{peak}} = 5.2\%$), and (d) 70% siltstone ($\varepsilon_a = 5\%$, $\varepsilon_a^{\text{peak}} = 4.7\%$). $\varepsilon_a^{\text{peak}}$ is the strain at which the peak stress is mobilized.
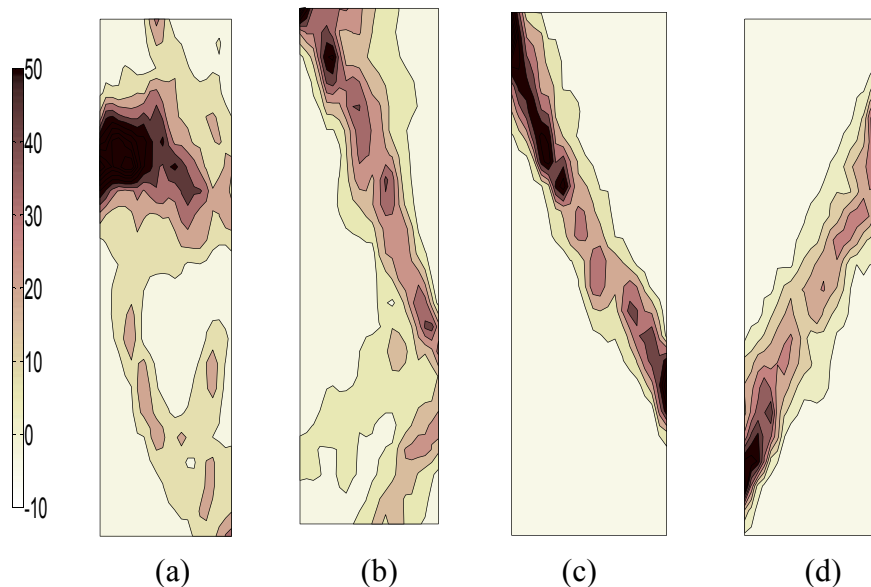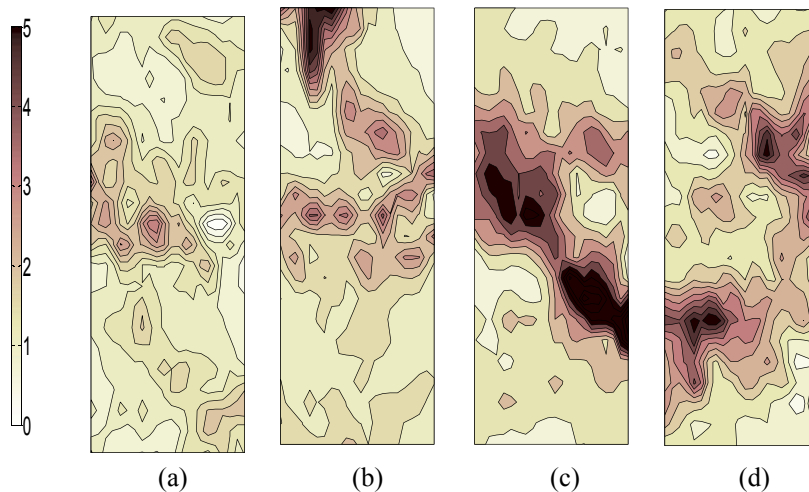

Fig. 7. Images of volumetric strain (given as %) at the end of tests with $q_{\text{strong}}^{\max}/q_{\text{weak}}^{\max} = 1.75$, where the darkest color gives the greatest rotation and color scaling is normalized for each plot: (a) 10% siltstone ($\varepsilon_a = 4\%$, $\varepsilon_a^{\text{peak}} = 3.8\%$), (b) 20% siltstone ($\varepsilon_a = 4.5\%$, $\varepsilon_a^{\text{peak}} = 4.3\%$), (c) 50% siltstone ($\varepsilon_a = 5.5\%$, $\varepsilon_a^{\text{peak}} = 5.2\%$), and (d) 70% siltstone ($\varepsilon_a = 5\%$, $\varepsilon_a^{\text{peak}} = 4.7\%$).
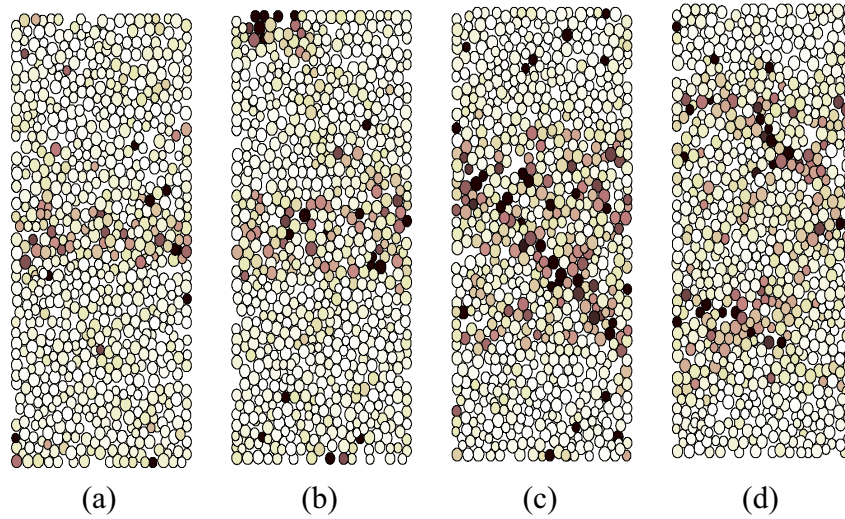
Fig. 8. Images of particle rotations close to the strain at which the peak stress is mobilized (ε_a^{peak}) for $q_{strong}^{max}/q_{weak}^{max} = 1.75$, where the darkest color gives the greatest rotation: (a) 10% siltstone ($\varepsilon_a = 4\%$, $\varepsilon_a^{peak} = 3.8\%$), (b) 20% siltstone ($\varepsilon_a = 4.5\%$, $\varepsilon_a^{peak} = 4.3\%$), (c) 50% siltstone ($\varepsilon_a = 5.5\%$, $\varepsilon_a^{peak} = 5.2\%$), and (d) 70% siltstone ($\varepsilon_a = 5\%$, $\varepsilon_a^{peak} = 4.7\%$).
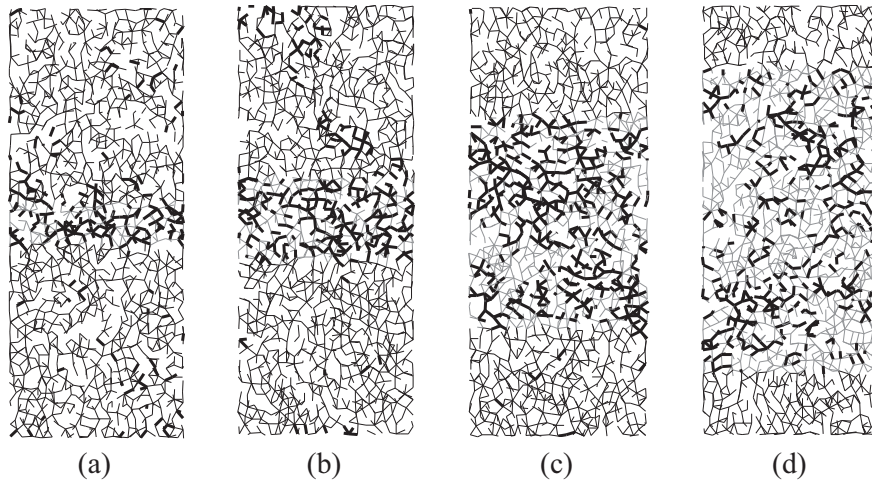
Fig. 9. Images of bonds close to the strain at which the peak stress is mobilized (ε_a^{peak}) for $q_{strong}^{max}/q_{weak}^{max} = 1.75$, where thin black lines represent intact sandstone bonds, thin grey lines represent intact siltstone bonds, thick black lines represent ruptured bonds: (a) 10% siltstone ($\varepsilon_a = 4\%$, $\varepsilon_a^{peak} = 3.8\%$), (b) 20% siltstone ($\varepsilon_a = 4.5\%$, $\varepsilon_a^{peak} = 4.3\%$), (c) 50% siltstone ($\varepsilon_a = 5.5\%$, $\varepsilon_a^{peak} = 5.2\%$), and (d) 70% siltstone ($\varepsilon_a = 5\%$, $\varepsilon_a^{peak} = 4.7\%$).

Fig. 10. Images of lateral strain (given as %) close to the strain at which the peak stress is mobilized (ε_a^{peak}) for $q_{strong}^{max}/q_{weak}^{max} = 1.75$: (a) 10% siltstone ($\varepsilon_a = 4\%$, $\varepsilon_a^{peak} = 3.8\%$), (b) 20% siltstone ($\varepsilon_a = 4.5\%$, $\varepsilon_a^{peak} = 4.3\%$), (c) 50% siltstone ($\varepsilon_a = 5.5\%$, $\varepsilon_a^{peak} = 5.2\%$), and (d) 70% siltstone ($\varepsilon_a = 5\%$, $\varepsilon_a^{peak} = 4.7\%$).

in Fig. 7, where the volumetric strain values were calculated using the wavelet-based method outlined in O'Sullivan et al. (2003). The results shown in Figs. 6 and 7 basically agree with the interpretation of Tziallas et al. (2013) at siltstone contents of 10% and 20% with the failure process clearly propagating from siltstone into sandstone. At a siltstone content of 50%, the failure does propagate into the sandstone, but only in the upper sandstone layer; whilst at a siltstone content of 70%, there is little evidence of failure in the sandstone.

6. Particle-scale analysis of gross yield

The DEM data enable analysis of the mechanisms associated with the onset of failure. Figs. 8–11 consider the same DEM specimens as in Figs. 6 and 7 at strain levels close to the one at which the peak deviatoric stress was mobilized. Again a slice through the center of the specimen is illustrated. Fig. 8 considers particle rotations (again these used to identify the localization) and Fig. 9 takes into account the intact and ruptured parallel bonds. Furthermore, Fig. 10 illustrates the lateral strains ($\varepsilon_{xx} + \varepsilon_{yy}$), while Fig. 11 considers the volumetric strains.

Comparing Figs. 6 and 8, there is some evidence of the subsequent localizations after the peak stress is mobilized; however, it is clear that at the failure point, most of the deformation is concentrated in the weaker material (siltstone) for all four specimens. The localization observed in the sandstone in the upper left hand corner of the specimen in Fig. 8b is most likely due to a local heterogeneity in material packing/bonding. In Fig. 8c, the localization is arguably more developed, but it is harder to define the peak at this siltstone content.

In Fig. 9, the bonds are illustrated as lines joining the center of bonded particles. The thin black lines represent the intact sandstone bonds, the thin grey lines indicate the intact siltstone bonds, and the thick black lines are the ruptured bonds. Intact siltstone bonds are illustrated in grey color and the lines are thinner, while the ruptured bonds are presented as black thicker lines. The ruptured bonds are analogous to micro fractures that would occur in a physical test. These ruptures are largely concentrated in the siltstone layer, with evidence of limited micro fracture in the sandstone at $sl = 10\%$ and 20%. It also suggests that the concentration of micro fractures (bond breakages per unit volume) decreases as the siltstone concentration increases: the presence of intact bond in the siltstone being clearer at $sl = 70\%$ compared with the case when $sl = 10\%$. This observation is confirmed by the data

concerning the percentage of bond breakages versus axial strain given in Fig. 12, in which the percentage of siltstone bonds broken at failure decreases roughly with increasing siltstone content. Comparing Figs. 12 and 2a, the axial strain at which the stress–strain response becomes noticeably nonlinear increases with increasing sl value, and so does the axial strain at which bond breakages initiate in the siltstone. This confirms a link between micro fracturing and nonlinearity of the stress–strain response.

The strain data presented in Figs. 10 and 11 give an additional insight. Referring firstly to Fig. 11, it is clear that the strain is globally compressive (i.e. negative), with the largest concentration of compressive strain, as would be expected, in the siltstone material. The lateral strain data presented in Fig. 10 indicate that while the volumetric strain is compressive, the lateral strain in the siltstone is extensive. This indicates that the Poisson's effect is greater in the siltstone than that in the sandstone. These observations are in agreement with the hypothesis of Tziallas et al. (2013) who proposed that the differences in Poisson's ratios would mean that the
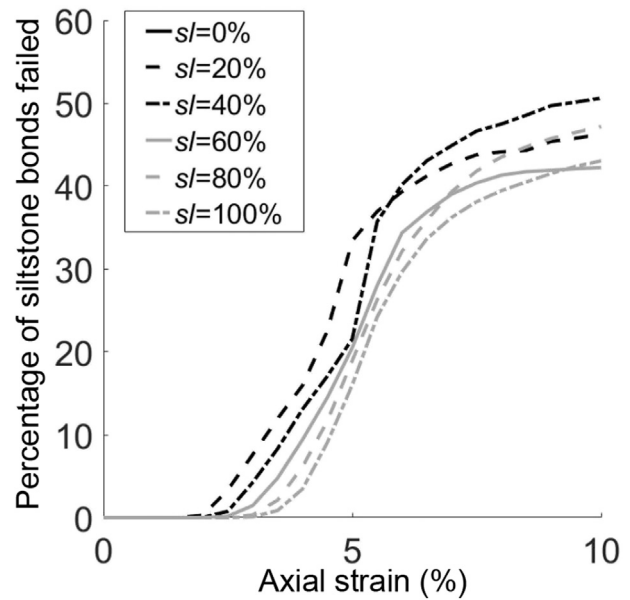

Fig. 12. Percentage of siltstone bonds broken at failure versus axial strain for $q_{\text{strong}}^{\max}/q_{\text{weak}}^{\max} = 1.75$.
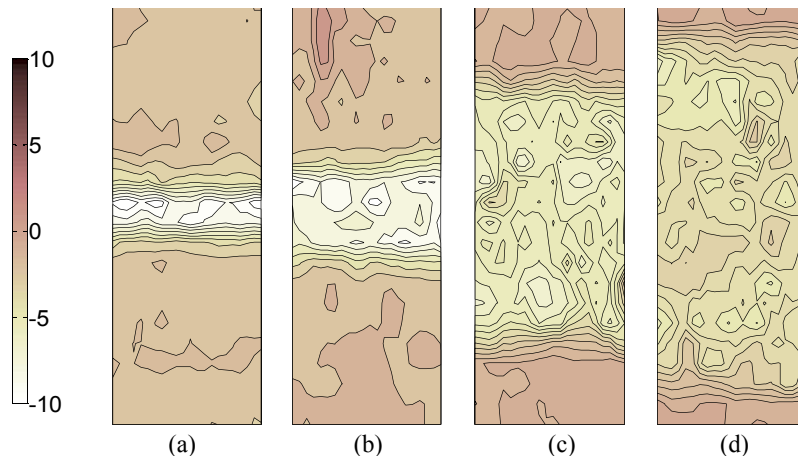

Fig. 11. Images of volumetric strain (ε_{vol}) (given as %) close to the strain at which the peak stress is mobilized ($\varepsilon_a^{\text{peak}}$) for $q_{\text{strong}}^{\max}/q_{\text{weak}}^{\max} = 1.75$: (a) 10% siltstone ($\varepsilon_a = 4\%$, $\varepsilon_a^{\text{peak}} = 3.8\%$), (b) 20% siltstone ($\varepsilon_a = 4.5\%$, $\varepsilon_a^{\text{peak}} = 4.3\%$), (c) 50% siltstone ($\varepsilon_a = 5.5\%$, $\varepsilon_a^{\text{peak}} = 5.2\%$), and (d) 70% siltstone ($\varepsilon_a = 5\%$, $\varepsilon_a^{\text{peak}} = 4.7\%$).

siltstone imposes a tensile (extensive) radial stress on the sandstone, while the sandstone in turn imposes a compressive radial stress on the siltstone. At the higher siltstone contents of $sl = 50\%$ and 70%, the extensive strains are concentrated in the regions that later emerge as localization zones (comparing Figs. 10 and 7).

7. Conclusions

The strengths of composite heterogeneous specimens depend on the percentage of the weaker material (siltstone) and are related to weaker material components, as predicted by both the laboratory study by Tziallas et al. (2013) and the present DEM simulations. In both cases, the strength decrease of the composite specimen with increasing percentage of the weaker material was greater than the strength decrease that one would expect from a simple linear weighting of the strengths of the two materials.

The strength reduction curves in the composite specimens, based on the laboratory tests, are divided into two distinct sections according to the failure mode (Tziallas et al., 2013): a declining curve for specimens with siltstone percentage up to 40% and a straight curve for specimens with siltstone percentage greater than 40%. The DEM simulation results using the BPM approach and PBM captured the general trends of the strength reduction curves, but it was impossible to observe the abrupt drop in the strength of the composite specimens at low values of siltstone percentage (between 30% and 40%) as observed in the laboratory tests. Instead the strength reduction was gentle, reaching the strength of the siltstone material at a percentage of 60%—80% (depending on the strength ratio of the stronger material to the weaker material). This difference can be attributed to the effect of the confining pressure.

For the DEM specimens, the stress—strain curve can be divided into two sections in the pre-peak region. The change in the slope of the stress—strain curves was attributed to the onset of breakage in the siltstone disc. The stiffness of composite specimens showed a gradual reduction with increasing proportion of the weaker material and agreed well with the laboratory test data. For the simulations presented in this study, the weaker layers were orthogonal to the major principal stress direction. However, future research should extend the earlier 2D contributions of Jeng et al. (2008) to consider layers inclined at a range of inclinations to the major principal stress.

Localization of strains was observed by considering the evolution of the parallel-bond network, the particle rotations and the local strain plots. Qualitative agreement was achieved between the failure patterns observed at the end of the physical tests and at the end of the numerical simulations. For example in both cases, damage was more clearly restricted to being within the siltstone zone as the siltstone percentage increased.

Overall the data presented here extend earlier 2D contributions to a more realistic 3D modeling scenario and support the use of PBM to simulate the failure behaviors of heterogeneous rocks.

Conflict of interest

The authors wish to confirm that there are no known conflicts of interest associated with this publication and there has been no significant financial support for this work that could have influenced its outcome.

References

Abe S, Urai JL. Discrete element modeling of boudinage: insights on rock rheology, matrix flow, and evolution of geometry. Journal of Geophysical Research: Solid Earth 2012;117(B1):1—13.

Cundall PA, Strack ODL. A discrete numerical model for granular assemblies. Géotechnique 1979;29(1):47—65.

Cho N, Martin CD, Sego DC. A clumped particle model for rock. International Journal of Rock Mechanics and Mining Sciences 2007;44(7):997—1010.

Cheung LYG, O'Sullivan C, Coop MR. Discrete element method simulations of analogue reservoir sandstones. International Journal of Rock Mechanics and Mining Sciences 2013;63:93—103.

Greco OD, Ferrero A, Pella D. Behavior of laboratory specimens composed by different rocks. In: 7th ISRM Congress; 1991. p. 241—5.

Hoek E. Brittle failure of rock. In: Rock mechanics in engineering practice. London: John Wiley and Sons; 1968. p. 99—124.

Hawkes I, Mellor M. Uniaxial testing in rock mechanics laboratories. Engineering Geology 1970;4(3):179—285.

Hsieh YM, Li HH, Huang TH, Jeng FS. Interpretations on how the macroscopic mechanical behavior of sandstone affected by microscopic properties-revealed by bonded-particle model. Engineering Geology 2008;99(1—2):1—10.

Jeng FS, Wang TT, Li HH, Huang TH. Influences of microscopic factors on macroscopic strength and stiffness of inter-layered rocks — revealed by a bonded particle model. Journal of Mechanics 2008;24(4):379—89.

Kwaśniewski M, Li X, Takahashi M. True triaxial testing of rocks. CRC Press; 2012.

Liang W, Yang C, Zhao Y, Dusseault MB, Liu J. Experimental investigation of mechanical properties of bedded salt rock. International Journal of Rock Mechanics and Mining Sciences 2007;44(3):400—11.

Lin H, Cao P, Wang Y. Numerical simulation of a layered rock under triaxial compression. International Journal of Rock Mechanics and Mining Sciences 2013;60:12—8.

Mohamed Z, Mohamed K, Cho GC. Uniaxial compressive strength of composite rock material with respect to shale thickness ratio and moisture content. Electronic Journal of Geotechnical Engineering 2007;13:1—10.

O'Sullivan C, Bray JD, Li S. A new approach for calculating strain for particulate media. International Journal for Numerical and Analytical Methods in Geomechanics 2003;27(10):859—77.

Potyondy DO, Cundall PA. A bonded-particle model for rock. International Journal of Rock Mechanics and Mining Sciences 2004;41(8):1329—64.

Paterson MS, Wong T. Experimental rock deformation — the brittle field. Springer; 2005.

Potyondy DO. Simulating stress corrosion with a bonded-particle model for rock. International Journal of Rock Mechanics and Mining Sciences 2007;44(5):677—91.

Park B, Min KB. Bonded-particle discrete element modeling of mechanical behavior of transversely isotropic rock. International Journal of Rock Mechanics and Mining Sciences 2015;76:243—55.

Tien YM, Kuo MC, Juang CH. An experimental investigation of the failure mechanism of simulated transversely isotropic rocks. International Journal of Rock Mechanics and Mining Sciences 2006;43(8):1163—81.

Tang C, Hudson JA. Rock failure mechanisms: explained and illustrated. CRC Press; 2010.

Tziallas GP, Saroglou H, Tsiambaos G. Determination of mechanical properties of flysch using laboratory methods. Engineering Geology 2013;166:81—9.

Vergara MR, Kudella P, Triantafyllidis T. Large scale tests on jointed and bedded rocks under multi-stage triaxial compression and direct shear. Rock Mechanics and Rock Engineering 2015;48(1):75—92.

Zhang Q, Zhu H, Zhang L, Ding X. Study of scale effect on intact rock strength using particle flow modeling. International Journal of Rock Mechanics and Mining Sciences 2011;48(8):1320—8.

Spyridon Liakas is currently a Geotechnical Engineer working for Arup. He graduated from Aristotle University of Thessaloniki in July 2013 with a bachelor degree in Civil Engineering. He continued his studies gaining a MSc and DIC with Distinction in Soil Mechanics and Business Management from Imperial College London. Spyridon is involved in a variety of geotechnical design works including earthworks, retaining structures and foundations. He is specialized in numerical modeling of soil-structure interaction and the use of advanced constitutive models.
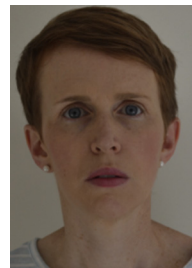
Dr. Catherine O'Sullivan is a Reader in Particulate Soil Mechanics in the Department of Civil and Environmental Engineering at Imperial College London, UK. Having completed her undergraduate and master's degrees at University College Cork, Ireland, she studied for her PhD at the University of California at Berkeley. From 2002 to 2004, she was a member of the academic staff at University College Dublin, Ireland. Dr. O'Sullivan's research focuses on the particle-scale interactions that underlie the mechanical behavior of soil. She has used both discrete element modeling and micro computed tomography in her research. Her recent work has focussed on critical state soil mechanics, small strain dynamic soil behavior and internal erosion. Dr. O'Sullivan has authored / co-authored over 70 peer-reviewed journal contributions and wrote a book about discrete element modeling. She is a member of the editorial panel of *Soils and Foundations* and the ASCE *Journal of Geotechnical and Geoenvironmental Engineering*.

Dr. Charalampos Saroglou is a Senior Teaching & Research Fellow in the School of Civil Engineering, National Technical University of Athens. He obtained a BSc in Geology from National University of Athens, a DIC. and MSc in Engineering Geology from Imperial College, U.K., a MSc in Design and Construction of Underground Works and a PhD in Engineering Geology – Rock Mechanics from National Technical University Athens, Greece, in 2007. From 2013 to 2014 he was Lecturer at the Department of Civil & Environmental Engineering in Imperial College and Visiting Lecturer from 2014 to 2016. He was a Visiting Professor in the Institute of Geology and Geophysics in the Chinese Academy of Sciences in 2016. He has received an Honor from the Academy of Athens in 2009 and the Richard Wolters Prize by the International Association of Engineering Geology and the Environment (IAEG) in 2012. His research interests include (1) the engineering behavior of rocks and rock masses, weak rocks and complex formations, (2) engineering geology of major infrastructure works, (3) tunneling and (4) mitigation of geohazards (landslides and rockfalls) and risk assessment. He is an Editorial Board Member in the *Bulletin of Engineering Geology* of IAEG.